SLAC-PUB-16237

Ultra-bright x-ray laser scattering for dynamic warm dense matter physics

L. B. Fletcher[1,2], H. J. Lee[1], T. Döppner[3], E. Galtier[1], B. Nagler[1], P. Heimann[1], C. Fortmann[4], S. LePape[3], T. Ma[3], M. Millot[2,3], A. Pak[3], D. Turnbull[3], D. A. Chapman[5,6], D. O. Gericke[5], J. Vorberger[7], T. White[8], G. Gregori[8], M. Wei[9], B. Barbrel[2], R. W. Falcone[2], C.-C. Kao[1], H. Nuhn[1], J. Welch[1], U. Zastrau[1,10], P. Neumayer[11], J. B. Hastings[1] and S. H. Glenzer[1]

[1]SLAC National Accelerator Laboratory, 2575 Sand Hill Road, MS 19, Menlo Park, CA 94025. [2]Physics Department, University of California Berkeley, Berkeley, CA 94709, USA. [3]Lawrence Livermore National Laboratory, P.O. Box 808, Livermore, CA 94551, USA. [4]QuantumWise A/S, Lersoe Parkalle 107, 2100 Koebenhavn, Denmark. Plasma Physics Group, [5]AWE plc, Aldermaston, Reading RG7 4PR, UK. [6]Centre for Fusion, Space and Astrophysics, Department of Physics, University of Warwick, Coventry CV4 7AL, UK. [7]Max Planck Institute for the Physics of Complex Systems, Noethnitzer Strasse 38, 01187 Dresden, Germany. [8]University of Oxford, Parks Road, Oxford, OX1 3PU, UK. [9]General Atomics, San Diego, CA. [10]Institute for Optics and Quantum Electronics, Friedrich-Schiller-University 07743 Jena, Germany, [11] GSI Helmholtzzentrum für Schwerionenforschung GmbH, Planckstraße 1 64291 Darmstadt, Germany.

In megabar shock waves, materials compress and undergo a phase transition to a dense charged-particle system that is dominated by strong correlations and quantum effects. This complex state, known as warm dense matter (*WDM*), exists in planetary interiors and many laboratory experiments, e.g., during high-power laser interactions with solids or the compression phase of inertial confinement fusion implosions. Here, we apply record peak brightness X rays at the Linac Coherent Light Source (*LCLS*) to resolve ionic interactions at atomic (Ångstrom) scale lengths and to determine the physical properties. Our *in situ* measurements characterize the compressed lattice and resolve the transition to WDM demonstrating that short-range repulsion between ions must be accounted for to obtain accurate structure factor and equation of state data. In addition, the unique properties of the x-ray laser provide plasmon spectra that yield temperature and density with unprecedented precision at micron-scale resolution in dynamic compression experiments.

Materials exposed to high pressures of one megabar and above have received increased recent attention due to their importance for the physics of planetary formation[1-3], material science[4], and inertial confinement fusion research[5]. The behaviour of shock-compressed aluminium is of particular interest because it has been proposed as a standard for shock wave experiments[6], and is widely used for equation-of-state[7,8] and *WDM*[9,10] studies. At room temperature, aluminium has three delocalised electrons thus it provides the prototype of an ideal electron fluid. As temperatures and pressures are increased, compressing and breaking ionic lattice bonds, still strong ionic forces are present which results in significant deviations from the simple fluid.

Density functional theory coupled to many particle molecular-dynamics (*DFT-MD*) simulations has evolved into an *ab initio* tool to explore this regime of high-pressure physics[11,12]. Up to now, these simulations were used to predict physical properties derived from optical observations of particle and shock velocities. On the other hand, studies of structural properties that are sensitive to many-particle electron-ion and ion-ion interaction physics[13] have been challenging[14]. Recent progress has been made using x-ray absorption spectroscopy[15,16]. Whilst early experiments on 4th generation light sources[17] have employed x-ray diffraction and measured the structural evolution from elastic to plastic states[18], reaching pressures in the Megabar regime, required for melting of many solids, has recently become available at the Matter in Extreme Conditions (*MEC*) instrument at *LCLS*.

Here we visualize, for the first time, the evolution of compressed matter across the melting line and the coexistence regime into a *WDM* state. The combination of high-power optical lasers with the x-ray beam at *MEC* provides high-resolution x-ray scattering at multi megabar pressures. Specifically, our data provide the ionic structure factor and determine pressures as function of density and temperature. In this regime, density and temperature characterization required the additional application of x-ray seeding a just recently invented tool[19]. In this study, we developed 8 keV peak brightness radiation of 2.7×10^{34} photons s^{-1} mm^{-2} $mrad^{-2}$ 0.1% bandwidth at *LCLS*, cf. Fig (1), to resolve collective electron excitations (plasmons) in forward scattering. The focussing capabilities at *MEC* allow these precision measurements with sub-micron focal spots. This is important for resolving physics on a scale length that occurs, e.g., in studies of material melting[20] (2 μm depth), for high energy-density plasmas produced by nanowires[21] (5 μm depth), or to resolve coalescing shock features[22] (10 μm scale length).

The experiment determines the structure factor during the short-lived high-pressure phase of the experiment revealing a narrow peak that reflects combined effects of screening and short-range repulsion in the ion-ion interaction potential. These results show differences from recently published structure factors[23,24]. Furthermore, our experimental and computational findings using *DFT-MD* are precise enough to allow for the direct calculation of macroscopic material properties. We present equation-of-state data on the shock Hugoniot together with new off-Hugoniot data that occur by shock coalescence. We find that they approach an isentrope and are in agreement with *DFT-MD* simulations performed for the measured temperature and density values of the experiment.

Published in the Nature Photonics, 23, March 2015, DOI: 10.1038/nphoton.2015.41

This material is based upon work supported by the U.S. Department of Energy, Office of Science, Office of Basic Energy Sciences, under Contract No. DE-AC02-76SF00515.

Shock-compressed Matter

The schematic of the experiment is shown in Fig. (2) together with data records from x-ray scattering detectors. The spectrometers have been fielded for density and temperature measurements from plasmons and angular resolved scattering provides diffraction and structure factor data. Here, two 4.5-J laser beams irradiate 50 μm thick Al foils (initial density of $\rho_{\square}$ = 2.7 g cm^{-3}) that are coated with 2 μm thick parylene. The laser beams are absorbed in the parylene, heat the material and launch two counter-propagating multi-megabar shock waves into the solid aluminium by ablation pressure. The laser power rises within 0.5 ns to a flat-in time power with intensities of 35 TW cm^{-2}. Each laser operates at 527 nm and is spatially smoothed[25] over a focal spot of 60 μm to launch strong shocks.

Radiation-hydrodynamic simulations using the code *HELIOS*[26] show that the shocks propagate inward at 14 km/s, each shock wave compressing the aluminium target to 4.5 g cm^{-3}. The shock speed and planarity over the central 10 μm-diameter region were verified by shock breakout measurements from 25 μm-thick foils irradiated by a single beam. Thus, when adding the second beam on the opposite side of the target, we doubled the foil thickness to 50 μm to mirror the shock propagation. When the shocks coalesce in the centre of the foil at 1.8 ns after the beginning of the laser drive, the density increases to 7 g cm^{-3} reaching peak pressures of 5 megabar. The 50 fs LCLS x-ray laser pulse at a photon energy of $E_0 = 8$ keV has been focused to a 10 μm spot penetrating into the dense compressed aluminium probing the conditions by x-ray scattering. The delay between the nanosecond optical driver beams and the x-ray laser beam has been varied and monitored with an accuracy of 0.05 ns, probing conditions before and during shock coalescence.

Plasmons

To resolve the electron plasma (Langmuir) oscillations[27], we operate *LCLS* in the seeded x-ray mode (see Methods). Without hard x-ray seeding, the aluminium plasmon spectra cannot be resolved, see Ref. [27] for more details. The Linac accelerates electrons with a single bunch charge of 150 pC to approximately 13.6 GeV electron beam energy. Within the first 15 undulators the Linac produces Self Amplified Spontaneous Emission (*SASE*) with 1 GW power. The electron beam is then passed through a 4 m long chicane while the x-ray beam traverses a diamond crystal that Bragg reflects a narrow energy range of x rays with a bandwidth of $\Delta E/E$ = 0.5 x 10^{-4} in the centre of the broad SASE spectrum. Thus, the transmitted x-ray spectrum creates a 5 MW trailing monochromatic seed pulse, which has been amplified to ultrahigh peak brightness and total power of 10-15 GW in the subsequent 17 undulators and focused into the dense laser-driven aluminium target.

Figure 3 shows the plasmon scattering spectra and theoretical fits of the dynamic structure factor $S(\boldsymbol{k},\omega)$ near peak-compression at t = 1.9 ns and from uncompressed aluminium. The plasmon feature is downshifted from the incident 8 keV x rays as determined by the generalized Bohm-Gross dispersion relation, see supplemental information, and its resonance frequency is used as a sensitive marker of the electron density. The data from uncompressed aluminium yield a total plasmon shift of 19 eV providing a free electron density of 1.8 x 10^{23} cm^{-3} that increases to 29 eV at shock coalescence. For the example shown in Figure 3, a density of 4.1 x 10^{23} cm^{-3} has been measured and corresponding to 2.3x compression. The error in electron density is ±5% determined by noise in the data and the fit of the theoretical dynamic structure factor.

The scattering spectra further provide a measure of the temperature by analysing the intensity of the elastic scattering features. For this purpose, structure factors are determined from wavenumber resolved scattering while the absolute intensity is determined by the intensity ratio with the plasmon feature; the plasmon intensity is determined by the *f*-sum rule (particle conservation)

$$\int_{-\infty}^{\infty} \left(\frac{\square^2\square}{\square\Omega\square\square}\right)_{\square\square\square\square\square\square\square} \square\square\square = \frac{\square\hbar\square^2}{2\square_{\square}}, \quad (1)$$

where $(d^2\sigma/d\Omega\, d\omega)_{\text{Plasmon}}$ is the measured plasmon intensity from the free electron Langmuir oscillations. Here, $Z = 3$ is the ion charge state, $\hbar$ is Planck's constant, k is the wavenumber and m_e the electron mass. At peak compression, the intensity of the elastic scattering feature increases by a factor of 2.8 over the cold scattering amplitude. We use a model[28] to fit the measured intensities; the potential and structure factors are shown in the supplemental information; they are in excellent agreement with our experimental data and simulations discussed further below. For the example shown in Fig. 3 we find a temperature of T = 20,000 K, i.e., 1.75 eV±0.5 eV. For our conditions, the ultrafast x-ray pulse deposits 3,500 K or 0.3 eV per electron into the target. A fraction of the energy can be expected to heat the electron fluid, but the total energy is small compared to shock heating and will not affect the plasmon shift. In addition, within the duration of the x-ray pulse, the ionic correlations have no time to respond to changes of the screening properties as demonstrated by the observation of solid and solid compressed states of aluminium.

X-ray Diffraction

Figure 4 shows the wavenumber resolved scattering data from which we obtain the high-pressure ion-ion structure factors. At $t=0$, before the rise of the optical laser beam power, the data show peaks from Debye-Scherrer rings indicating the ionic lattice in the solid. The peaks at 38°, 45°, and 65° correspond to (111), (200), and (220), respectively. When the shocks are launched and compress the solid, the lattice spacing d is reduced and we observe that the peaks shift to larger scattering angles as determined by the Bragg scattering equation $n\lambda_{x\text{-}ray} = 2d \sin\theta$, here $\lambda_{x\text{-}ray}$

= 1.55 Å the wavelength of the incident x-ray laser, and 2θ the scattering angle.

With increasing laser energy we access higher pressures, the aluminium melts and transitions into the warm dense matter state. We first observe a comparatively broad ion-ion correlation peak at an angle of 45˚ at 1.38x compression together with shifted Bragg scattering of solid compressed aluminium. For these conditions the comparison with simulations shows that the wave number of both the ion-ion correlation peak and the shifted Bragg peak provide the same density indicating a co-existence regime. With higher pressure accessed later in time and with higher laser intensity, we compress aluminium up to 1.9x the initial density and the strong ion-ion correlation peak shifts to 2θ = 51˚. At shock coalescence, the peak shifts further to 2θ = 55˚ and the data indicate 2.3x compressed aluminium consistent with densities inferred from the simultaneous measurements of the plasmon shift.

The measured ion-ion correlation feature is sensitive to the ion-ion structure factor[29]. For nearly elastic scattering the scattering angle 2θ determines the wavenumber of the correlations. With $\boldsymbol{k} = 2\boldsymbol{k}_{x\text{-}ray} \sin\theta$ and $k = 2\pi/\lambda$ determining the scale length of the density fluctuations measured in this scattering experiment, we find 1.38 Å < λ_{SL} < 5.7 Å. On these atomic scale lengths, the scattering amplitude is probing important details of the ion-ion interaction potential V_{ii}.

Discussions

In Figure 4 we compare the measured ion-ion correlation feature with various theoretical approximations. We find that the data depend on both material compression and on the choice of the interaction potential. Using densities and temperatures derived from the plasmon spectra we find excellent agreement of the measured wavenumber-resolved scattering data with *DFT-MD* simulations (see Methods).

The physical picture evolves as follows: effective ion-ion pair potentials are directly extracted from the *DFT-MD* simulations by matching the pair correlation function g(r). This potential can be matched to a short-range-repulsion model (*SRR*) that modifies screened Coulomb interactions in ionized matter. The potential can be described as

$$\varphi_{ii}(r) = \frac{Z^2 e^2}{4\pi\varepsilon_0 r} e^{-\kappa r} + \frac{\sigma^4}{r^4}, \qquad (2)$$

with r being the distance between ions, k_B is Boltzmann's constant, e the electron charge number, $\kappa = \kappa(n_e, T_e)$ is the Yukawa screening function. For our conditions, κ approaches the Thomas-Fermi screening length with accuracy of better than 1%. The last term in Eq. (2) accounts for the additional repulsion from overlapping bound electron wave functions, with the parameter $\sigma = 9.4a_B$ fitted to match *DFT-MD* simulations[30].

The interaction potential, Eq. (2), determines the shape of the wavenumber resolved scattering data and the angle of the maximum scattering amplitude; the latter is further sensitive to the density. Figure 4 (top three panels) shows that the *DFT-MD* simulations, Eq. (2), and the wavenumber resolved scattering data agree well with each other for densities obtained independently from the plasmon or Bragg scattering data.

These results further provide constraints on structure factor models that can be applied in theoretical fitting of scattering spectrum and to determine temperatures from scattering amplitudes. Importantly, linearly screened Coulomb potentials, denoted here by Yukawa in Fig. 4, show no agreement with our results, see supplementary information.

Our experimental and theoretical structure factors further allow us to determine the material properties at high density and high pressures. In particular, the measured wavenumber resolved scattering data $W(\boldsymbol{k})$ yield the structure factor $S(\boldsymbol{k})$ using $W(k) = S(k)[f(k)+q(k)]^2$ with the atomic form factor $f(k)$ and the screening function $q(k)$[31,32] that can be integrated and which provides a novel method for determining the pressure. The total pressure consists of ionic and electronic contributions with $P_{tot} = P_i + P_e$. In nearly Fermi degenerate conditions, P_e includes well-known density-sensitive contributions accounting for Fermi pressure, degeneracy, Coulomb, and exchange terms[33]. On the other hand, the ion pressure, when divided into an ideal gas part $P_G = n_i k_B T$ and the correlation part $P_i = p^x + P_G$, is dominated by the (negative) ion excess pressure

$$\frac{U^{ex}}{N} = \frac{3}{2}k_B T - \frac{2\pi n_i (Ze)^2}{3} \int_0^\infty g(r) \frac{r^4}{(r^2+\sigma^2)^2} dr \qquad (3)$$

with U/N being the internal energy. In Eq. (3), we may use the structure factor directly obtained from the measured wavenumber resolved scattering data.

Figure 5 compares the experimental pressure data with available empirical data[6] and state-of-the-art simulations. In particular, we show previous *DFT-MD* simulations for temperatures calculated for the shock Hugoniot[34] together with our *DFT-MD* simulations performed for temperatures and densities of the present experiment[35]; the latter provides excellent agreement with the data. Our data further show no indication of Bragg peaks for compressed aluminium above P = 1.2 Mbar consistent with previous melt line measurements on the Hugoniot[36]. Our present data set extends further showing the disappearance of Bragg scattering data above 1.2 Mbar and up to densities of 4.5 g/cc. At higher pressures, the shock coalescence data are on the isentrope[37,38] slightly above the isotherm[6] validating our understanding of dense aluminium utilizing pressure, temperatures and densities solely based on measurements.

Our findings demonstrate that spectrally and wavenumber resolved x-ray scattering is applicable for thorough testing of radiation-hydrodynamic calculations and equation of state models. Our methods present unique highly resolved data for dynamic high-pressure material science studies that require accurate knowledge of material properties at high densities and are applicable for future studies aimed at observing effects of ionization on the equation of state at

high compression. Only the unique properties of the seeded x-ray laser at *LCLS* provide the accuracy of data needed to distinguish between theories and simulations on a microscopic level.

Methods

The initial proposal for hard x-ray self-seeding at *LCLS* was described in reference 19. The forward Bragg scattered beam consists of a 'prompt' transmitted beam and a delayed monochromatic wake generated from the wings of the Bragg diffraction profile. The diamond (400) reflection was chosen as the wake monochromator for suitable crystal perfection, angular width and low absorption. The approach to self-seeding matched the electron bunch duration of approximately 10 fs (20 pC) to the width of the first wake maxima. The operational phase, following commissioning of self-seeded operation, has shown that the normal operation of hard x-ray self-seeding performs better with the nominal 150 pC charge and the corresponding 50 fs pulse duration. The stability is improved by roughly a factor of two compared to the low charge operation with a similar reduction in the per pulse energy fluctuations. In this mode the pulse energy of the seeded beam is significantly improved with the longer pulse (higher charge) mode. The seeded beam normally gives a 2 to 4 times improvement in time average x-ray power compared with a post-monochromator of similar bandwidth with similar pulse durations and shot-to-shot intensity fluctuations. The narrow seeded line, 0.4 to 1.1 eV full-width at half maximum, for a 50 fs pulse duration typically contains an average pulse energy of 0.3 mJ, with occasional shots up to 1 mJ. The peak brightness of 2.7x10^34 photons/s/mm^2//mrad^2 0.1% BW is calculated from the measured pulse duration and a mean pulse energy of 0.3 mJ.

The *DFT-MD* simulations of this study were performed using the code *VASP*[38-41]. The exchange correlation functional has been approximated with the generalised gradient approach[42,43] and the electron-ion pseudo-potential was taken within the projector augmented plane wave formalism[44,45]. Three electrons per atom are treated as valence electrons using a plane wave expansion; the 10 core electrons are treated with the projector augmented wave functions formalism. The core radius is $r_C = 1.7a_B$ with $a_B = 0.53$ *Å*. The Mermin functional accounts for thermal excitations. The electronic cut off for the plane wave representation of the wave function is set to 550 eV as tested to provide the free energy and pressure with about 0.7 % accuracy.

The simulations have been performed in a super-cell with constant number of particles, volume and temperature with periodic boundary conditions. Here, the temperature of the nuclei is controlled by means of a Nose thermostat[46,47]. We use N =256 ions for the fluid. Initial runs have been performed at lower temperatures starting with the ions in an fcc lattice at the appropriate densities of the experiment. The resulting ionic configurations were then used as starting configurations for runs at the temperatures of interest. The Brillouin zone sampling has been validated by running part of each *DFT-MD* run with a 2 × 2 × 2 Monkhorst-Pack k-point grid instead of just the Γ-point[48]. Pressure differences of about 0.5 % have been found. We used a 0.2 fs time step run the simulations for 2000 to 23000 steps. An initial relaxation time of varying length was excluded from the analysis of the equation of state.

References and Notes

1. Ross, M. The ice layer in Uranus and Neptune—diamonds in the sky? *Nature* **292**, 435-436 (1981).
2. Benedetti, L. R., Nguyen, J. H., Caldwell, W. A., Hongjian, L., Kruger, M., & Jeanloz, R. Dissociation of CH_4 at High Pressures and Temperatures: Diamond Formation in Giant Planet Interiors? *Science* **286**, 100 -102 (1999).
3. Coppari, F., Smith, R. F., Eggert, J. H., Wang, J., Rygg, R. J., Lazicki, A., Hawreliak, J. A., Collins, G. W. & Duffy, *T. S.* Experimental evidence for a phase transition in magnesium oxide at exoplanet pressures. *Nature Geoscience* **6**, 926–929 (2013).
4. Ernstorfer R., Harb M., Hebeisen C. T., Sciaini G., Dartigalongue T., and Miller, R. J. D. The Formation of Warm Dense Matter: Experimental Evidence for Electronic Bond Hardening in Gold. *Science* **323**, 1033 -1037 (2009).
5. Glenzer, S. H., MacGowan, B. J., Michel, P., Meezan, N. B., Suter, L. J., Dixit, S. N., Kline, J. L., Kyrala, G. A., Bradley, D. K., Callahan, D. A., Dewald, E. L., Divol, L., Dzenitis, E., Edwards, J. E., Hamza, A. V., Haynam, C. A., Hinkel, D. E., Kalantar, D. H., Kilkenny, J. D., Landen, O. L., Lindl, J. D., LePape, S. Moody, J. D., Nikroo, A., Parham, T., Schneider, M. B., Town, R. P. J., Wegner, P., Widmann, K., Whitman, P., Young, B. K. F., Van Wonterghem, B., Atherton, L. J. & Moses E. I. Symmetric Inertial Confinement Fusion Implosions at Ultra-High Laser Energies, Science **327**, 1228-1231 (2010).
6. Young, D. A., Wolford, J. K., Rogers, F. J. & Holian K. S. Theory of the aluminum shock equation of state to 10^4 Mbar. *Phys. Lett.* **108**, 157 - 160 (1985).
7. Ma, *T.*, Döppner, T., Falcone, R. W., Fletcher L., Fortmann C., Gericke, D. O., Landen, O. L., Lee, H.-J., Pak, A., Vorberger, J., Wünsch, K., & Glenzer S. H. X-Ray Scattering Measurements of Strong Ion-Ion Correlations in Shock-Compressed Aluminum. *Phys. Rev. Lett.* **110**, 065001 (2013).
8. Ravasio, A., Gregori, G., Benuzzi-Mounaix, A., Daligault, J., Delserieys, A., Faenov, A. Ya., Loupias, B., Ozaki, N., Rabec le Gloahec, M., Pikuz, T. A., Riley, D., & Koenig, M. Direct Observation of Strong Ion Coupling in Laser-Driven Shock-Compressed Targets. *Phys. Rev. Lett.* **99**, 135006 (2007).
9. Ciricosta, O. *et al.* Direct Measurements of the Ionization Potential Depression in a Dense Plasma. *Phys. Rev. Lett.* **109**, 065002 (2012).
10. Nagler, B. *et al.* Turning solid aluminium transparent by intense soft X-ray photoionization. *Nature Phys.* **5**, 693 (2009).
11. Focher P.,Chiarotti1 G. L., Bernasconi1 M., Tosatti E. and Parrinello M. Structural Phase Transformations via First-Principles Simulation, *Europhys. Lett*. 26 345 (1994).
12. Driver K. P. & Militzer B. All-electron path integral Monte Carlo simulations of warm dense matter: Application to water and carbon plasmas. *Phys. Rev. Lett.* **108**, 115502, (2012).
13. Garcia Saiz, E., Gregori, G., Gericke, D. O., Vorberger, J., Barbrel, B., Clarke, R. J., Freeman, R. R., Glenzer, S. H., Khattak, F. Y., Koenig, M., Landen, O. L., Neely, D., Neumayer, P., Notley, M. M., Pelka, A., Price, D., Roth, M., Schollmeier, M., Spindloe, C., Weber, R. L., van Woerkom, L., Wünsch, K., & Riley, D. Probing warm dense lithium by inelastic X-ray scattering. *Nature Phys.* **4**, 940-944 (2008).

14. Louis, A. A. & Ashcroft, N. W. Extending Linear Response: Inferences from Electron-Ion Structure Factors. *Phys. Rev. Lett.* **81**, 4456 (1998).
15. Benuzzi-Mounaix A., Dorchies A. F., Recoules V., Festa F., Peyrusse O., Lévy A., Ravasio A., Hall T., Koenig M., Amadou N., Brambrink E., & Mazevet S. Electronic Structure Investigation of Highly Compressed Aluminum with K Edge Absorption Spectroscopy. *Phys. Rev. Lett.* **107**, 165006 (2011).
16. Lévy A., Dorchies A. F., Benuzzi-Mounaix A., Ravasio A., Festa F., Recoules V., Peyrusse O., Amadou N., Bambrink E., Hall T., Koenig M., & Mazevet X-Ray Diagnosis of the Pressure Induced Mott Nonmetal-Metal Transition. *Phys. Rev. Lett.* **108**, 055002 (2012).
17. Emma, P., Akre, R., Arthur, J., Bionta, R., Bostedt, C., Bozek, J., Brachmann, A., Bucksbaum, P., Coffee, R., Decker, F.-J., Ding, Y., Dowell, D., Edstrom, S., Fisher, A., Frisch, J., Gilevich, S., Hastings, J., Hays, G., Hering, Ph., Huang, Z., Iverson, R., Loos, H., Messerschmidt, M., Miahnahri, A., Moeller, S., Nuhn, H.-D., Pile, G., Ratner, D., Rzepiela, J., Schultz, D., Smith, T., Stefan, P., Tompkins, H., Turner, J., Welch, J., White, W., Wu, J., Yocky, G. & Galayda, J. First lasing and operation of an ångstrom-wavelength free-electron laser. *Nature Photonics* **4**, 641-647 (2010).
18. Milathianaki, D., Boutet, S., Williams, G., J., Higginbotham, A., Ratnet, D., Gleason, A. E., Messerschmidt, M., Seibert, M. M., Swift, D. C., Hering, P., Robinson, J., White, W. E. & Wark J. S. Femtosecond Visualization of Lattice Dynamics in Shock-Compressed Matter. *Science* **342** 220-223 (2013).
19. Amann, J., Berg, W., Blank, V., Decker, F.-J., Ding, Y., Emma, P., Feng, Y., Frisch, J., Fritz, D., Hastings, J., Huang, Z., Krzywinski, J., Lindberg, R., Loos, H., Lutman, A., Nuhn, H.-D., Ratner, D., Rzepiela, J., Shu, D., Shvyd'ko, Yu., Spampinati, S., Stoupin, S., Terentyev, S., Trakhtenberg, E., Walz, D., Welch, J., Wu, J., Zholents, A., & Zhu, D. Demonstration of self-seeding in a hard-X-ray free-electron laser. *Nature Photonics* **6**, 693 – 698 (2012).
20. Boehler R. Temperatures in the Earth's core from melting-point measurements of iron at high static pressures. *Nature* **363**, 534-536 (1993).
21 Purvis M. A., Shlyaptsev V. N., Hollinger R., Bargsten C., Pukhov A., Prieto A., Wang Y., Luther B. M., Yin L., Wang S. and Rocca J. J. Relativistic plasma nanophotonics for ultrahigh energy density physics, *Nature Photonics* **7**, 796-800 (2013).
22. Kritcher, A. L., Neumayer, P., Castor, J., Döppner, T., Falcone, R. W., Landen, O. L., Lee, H.-J., Lee, R. W., Morse, E. C., Ng, A., Pollaine, S., Price, D. & Glenzer, S. H. Ultrafast X-ray Thomson Scattering of Shock-Compressed Matter. *Science* **322** 69-71 (2008).
23. Souza A. N., Perkins D. J., Starrett C. E., Saumon D. & Hansen S. B. Predictions of x-ray scattering spectra for warm dense matter. *Phys. Rev. E* **89**, 023108 (2014).
24. Rüter H. R. & Redmer R. Ab Initio Simulations for the Ion-Ion Structure Factor of Warm Dense Aluminum. *Phys. Rev. Lett.* **112**, 145007 (2014).
25. Dixit, S. N., Lawson, J. K., Manes, K. R., Powell, H. T. & Nugent, K. A. Kinoform phase plates for focal plane irradiance profile control. *Opt. Lett.* **19**, 417-419 (1994).
26. MacFarlane, J. J., Golovkin, I. E. & Woodruff, P. R. HELIOS-CR A 1-D radiation-magnetohydrodynamics code with inline atomic kinetics modeling, *Journal of Quantitative Spectroscopy and Radiative Transfer* **99**, 381-397 (2006).
27. Fletcher L. B., Galtier E., Heimann P., Lee H.-J., Nagler B., Welch J., Zastrau U., Hastings J. B., & Glenzer S. H. Plasmon measurements with a seeded x-ray laser. *Journal of Instrumentation* **8**, C11014 (2013).
28. Gregori G., Glenzer S. H. & Landen O. L. Generalized x-ray scattering cross section from non-equilibrium solids and plasmas, *Phys. Rev. E* **74** 026402 (2006).
29. Gericke, D. O., Vorberger, J., Gregori, G., & Wünsch, K. Screening of ionic cores in partially ionized plasmas within linear response. *Phys. Rev. E* 81, 065401(R) (2010).
30. Wünsch, K., Vorberger, J., & Gericke, D.O. Ion Structure in Warm Dense Matter: Benchmarking hypernetted-chain equations by first-principle simulations**.** *Phys. Rev. E* **79**, 010201(R) (2009).
31. Chihara J. Difference in x--ray scattering between metallic and non--metallic liquids due to conduction electrons, *J. Phys. F: Met. Phys.* **17**, 295 (1987).
32. Gregori G., Glenzer S. H., Rozmus W., Lee R. W. & Landen O. L. Theoretical model of x-ray scattering as a dense matter probe, *Phys. Rev. E*. **67,** 026412 (2003).
33. Salpeter, E. E. Energy and pressure of a zero-temperature plasma. *Astrophys. J*. **134**, 669 (1961).
34. Mazevet, S. & Zerah, G. *Ab Initio* Simulations of the *K* -Edge Shift along the Aluminum Hugoniot. *Phys. Rev. Lett.* **101**, 155001 (2008).
35. Vorberger, J., Donko, Z., Tkachenko, I. M. & Gericke, D. O. Dynamic Ion Structure Factor of Warm Dense Matter. *Phys. Rev. Lett.* **109**, 065002 (2012).
36. Ross M., Yang Linb H. & Boehler R. Melting of aluminum, molybdenum, and the light actinides. *Phys. Rev. B* **70**, 184112 (2004).
37. Davis, J.-P. Experimental measurement of the principal isentrope for aluminum 6061-T6 to 240GPa. J. *Appl. Phys.* **99**, 103512 (2006).
38. Kresse G. & Hafner J. *Ab initio* molecular dynamics for liquid metals. *Phys. Rev. B* **47**, 558 (1993).
39. Kresse G. & Hafner J. *Ab initio* molecular-dynamics simulation of the liquid-metal–amorphous-semiconductor transition in germanium. *Phys. Rev. B* **49**, 14251 (1994).
40. Kresse G. & Furthmüller J. Efficiency of *ab-initio* total energy calculations for metals and semiconductors using a plane-wave basis set. *Comput. Mat. Sci*. **6**, 15 (1996).
41. Kresse G. & Furthmüller J. Efficient iterative schemes for *ab initio* total-energy calculations using a plane-wave basis set. *Phys. Rev. B* **54**,11169 (1996).
42. Perdew J. P., Burke K. & Ernzerhof M. Generalized Gradient Approximation Made Simple. *Phys. Rev. Lett*. **77**, 3865 (1996).
43. Perdew J. P., Burke K. & Ernzerhof M. Generalized Gradient Approximation Made Simple. *Phys. Rev. Lett*. **78**, 1396 (1997).
44. Blöchl P. E. Projector augmented-wave method. *Phys. Rev. B* **50**, 17953 (1994).
45. Kresse G. & Joubert D. From ultrasoft pseudopotentials to the projector augmented-wave method. *Phys. Rev. B* **59**, 1758 (1999).
46. Nose S. J. A unified formulation of the constant temperature molecular-dynamics methods. *Chem. Phys.* **81**, 511 (1984).
47. Nose S. Constant temperature molecular dynamics methods. *Prog. Theor. Phys. Suppl*. **103**, 1 (1991).
48. Monkhorst H. J. & Pack J. D. On Special Points for Brillouin Zone Integrations. *Phys. Rev. B* **13**, 5188 (1976).

Acknowledgements

This work was performed at the Matter at Extreme Conditions (MEC) instrument of LCLS, supported by the DOE Office of Science, Fusion Energy Science under contract No. SF00515. This work was supported by DOE Office of Science, Fusion Energy Science under FWP

100182, and partially supported by DOE Office of Basic Energy Sciences, Materials Sciences and Engineering Division, under Contract DE-AC02-76SF00515. Part of this work was performed under the assistance of the U.S. Department of Energy by Lawrence Livermore National Laboratory under Contract DE-AC52-07NA27344. This work was further supported by Laboratory Directed Research and Development grant 11-ERD-050, and the Peter-Paul-Ewald Fellowship of the VolkswagenStiftung.

Author contributions

LBF and SHG co-wrote the manuscript. LBF, HJL, TD, EG, BN, PH, SLP, TM, AP, DT, TW, MW, BB, UZ, JBH and SHG performed the experiment. UZ, TD and HJL developed and commissioned the spectrometer. LBF, AP. analysed the spectra. CF, MM, DAC, DOG, JV, and GG performed calculations and simulations. LBF, TD, MM, DAC DOG, JV, GG, RWF, CCK, HN, JW, PN, JBH and SHG conceived the experiment and interpreted the results.

Additional information

Supplementary information is available in the online version of the paper. Correspondence and requests for materials should be addressed to LBF.

Competing financial interests

The authors declare no competing financial interests.

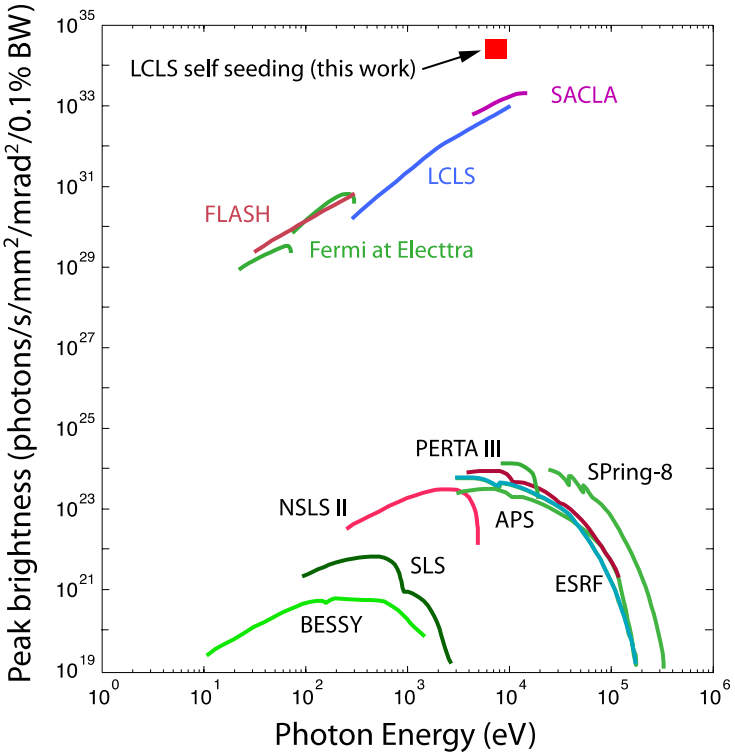

Figure 1 | Peak brightness. Comparison of peak brightness of various x-ray light sources is shown. In this study an internally seeded beam at high peak brightness provided the required resolution for resolving plasmons. For comparison, Fermi is an externally seeded free-electron laser.

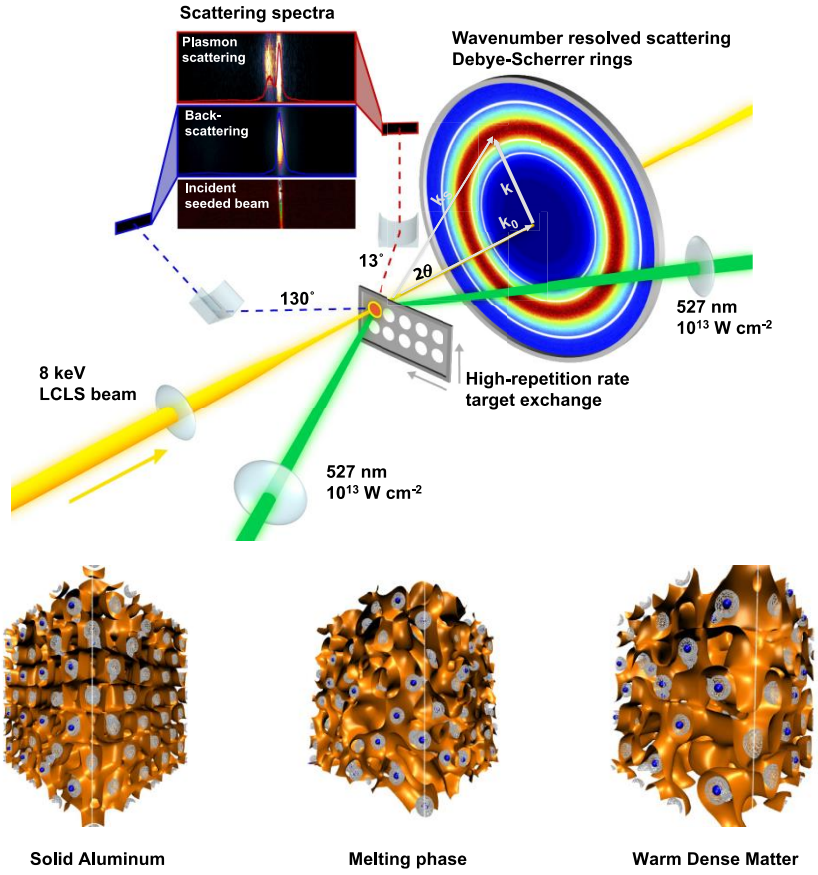

Figure 2 | WDM Experiment. (Top) A schematic of experimental setup at the Matter in Extreme Conditions (*MEC)* instrument at *LCLS is shown*. The short (50 fs), mono-energetic ($\Delta E/E_0 = 0.5 \times 10^{-4}$), ultra high brightness x-ray beam is focused into the dense laser-compressed aluminium target. The 13˚ forward x-ray scattering spectrum shows inelastic plasmon scattering together with the elastic scattering feature at the incident x-ray energy. The 130˚ backscattering shows no scattering feature in this energy range validating the identification of the plasmon. A CSPAD area detector observes the total wavenumber-resolved x-ray scattered intensity indicating the transition from Debye-Scherrer diffraction rings (white) to an intense ion-ion correlation scattering feature (red). (Bottom) DFT-MD simulations of the formation of WDM indicate that the ions (blue) abandon their lattice positions. Whilst core electrons (grey) remain mostly unchanged the delocalized conduction electrons (represented by orange isosurfaces) are disturbed from the very regular structure in the lattice.

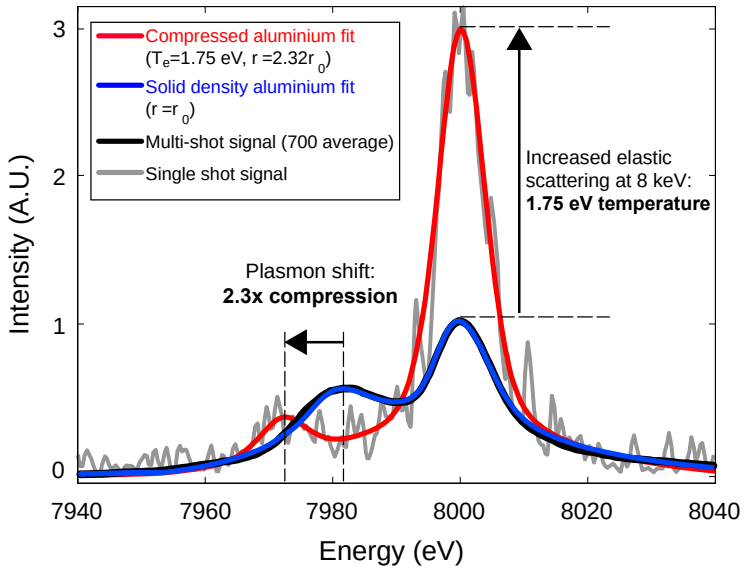

Figure 3 | Plasmon spectra. Comparison of the x-ray scattering spectra from compressed and solid-density aluminium showing the increase in plasmon frequency shift and elastic Rayleigh scattering amplitude with compression. The experimental data (black curves) are fitted with theoretical dynamic structure factor calculations (red and blue curves). The elastic scattering amplitude provides the temperature of 1.75 eV. The plasmon shift $\hbar\omega$ is determined by the Bohm-Gross dispersion relation with the plasma frequency being the leading term, thus $\hbar\omega \sim \hbar\omega_{pe} = \hbar\left(\frac{n_e e^2}{\varepsilon_0 m_e}\right)^{1/2}$ measuring the electron density n_e. In this example, the plasmon shift indicates material compression of 2.3 times solid density with ρ = 6.3 g/cm^3.

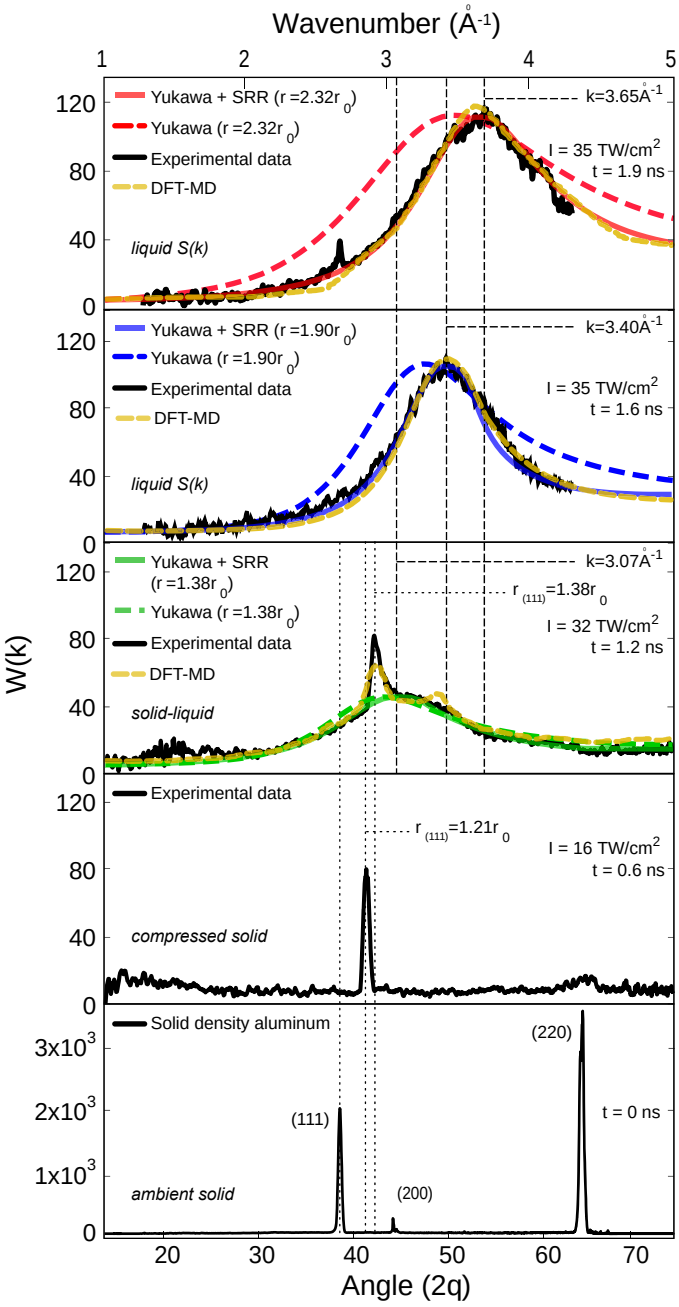

Figure 4 | Wave-number resolved scattering data. (Bottom) Bragg peaks from Debye-Scherrer rings are shown at t = 0 ns. (2nd from bottom) Data from compressed solid aluminium show a shift of the (111) Bragg peak by 3˚ and compression of 1.21 ρ_0. (Middle) Appearance of a broad ion-ion correlation peak is observed together with a Bragg peak shifted further to larger angles. (2nd from top) At higher compression, aluminium melts, Bragg peaks disappear, and the ion-ion correlation peak shifts to 50˚. (Top) The angle of the correlation peak increases further to 56˚ when higher densities are reached after coalescence. The data (black curves) show excellent agreement with *DFT-MD* simulations (top three panels). The data can also be described by a model that accounts for both Yukawa screening and short-range repulsion (red, blue and green solid curves), but a Yukawa-screened potential alone is not sufficient (dashed curves).

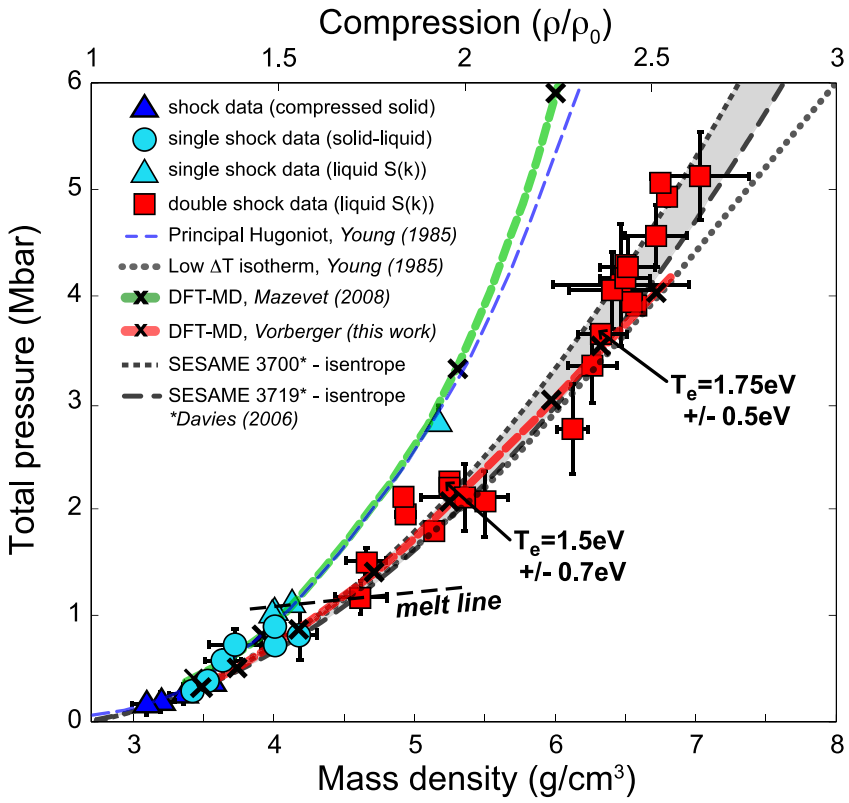

Figure 5 | Pressure-Density diagram. Comparison of pressure data of compressed dense aluminium measured for varying laser intensity is shown from single shocks and during shock coalescence of two counter-propagating shock waves. The single shock data follow the shock Hugoniot and *DFT-MD* simulations from ρ = 3.5 g/cm^3 to about ρ = 4 g cm^{-3} when the shock waves coalesce and the pressure values approach an isentrope (above the ΔT=0 isotherm) to ρ = 7 g/cm^3. The melt line (dashed) indicates the complete disappearance of shifted Bragg peaks in the wavenumber scattering measurements. The *DFT-MD* simulations of this work show excellent agreement when using the measured density and temperature data.